

# Theoretical Study of Conversion and Decay Processes of Excited Triplet and Singlet States in a Thermally Activated Delayed Fluorescence Molecule

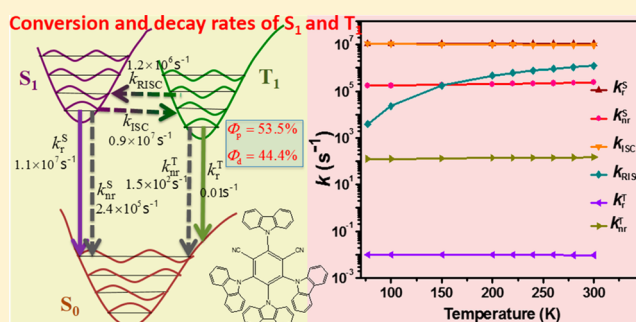
Qian Peng,<sup>†</sup> Di Fan,<sup>†</sup> Ruihong Duan,<sup>†</sup> Yuanping Yi,<sup>\*,†</sup> Yingli Niu,<sup>†</sup> Dong Wang,<sup>‡</sup> and Zhigang Shuai<sup>\*,‡</sup>

<sup>†</sup>Beijing National Laboratory for Molecular Sciences, CAS Key Laboratory of Organic Solids, Institute of Chemistry, Chinese Academy of Sciences, Beijing 100190, China

<sup>‡</sup>Key Laboratory of Organic Optoelectronics and Molecular Engineering, Department of Chemistry, Tsinghua University, Beijing 100084, China

## Supporting Information

**ABSTRACT:** Quantitative understanding of the photophysical processes is essential for developing novel thermally activated delayed fluorescence (TADF) materials. Taking as an example 1,2,3,5-tetrakis(carbazol-9-yl)-4,6-dicyanobenzene, a typical TADF-active molecule, we calculated the interconversion and decay rates of the lowest excited singlet and triplet states at different temperatures as well as the prompt and delayed fluorescence efficiencies at 300 K at the first-principles level. Our results can reproduce well the experimentally available data. It is found that the reverse intersystem crossing rate ( $k_{\text{RISC}}$ ) is sharply increased by 3 orders of magnitude, while the other rates increase slightly or remain unchanged when the temperature rises from 77 to 300 K. Importantly,  $k_{\text{RISC}}$  reaches up to  $1.23 \times 10^6 \text{ s}^{-1}$  and can compete with the radiative and nonradiative decay rates of  $S_1$  ( $1.11 \times 10^7$  and  $2.37 \times 10^5 \text{ s}^{-1}$ ) at 300 K, leading to an occurrence of delayed fluorescence. In addition, our calculations indicate that it is the freely rotational motions of the carbazolyl between two cyano groups that are responsible for the interconversion between  $S_1$  and  $T_1$ . The large torsional barriers of other three adjacent carbazolyl groups block the nonradiative decay channels of  $S_1 \rightarrow S_0$ , leading to strong fluorescence. This work would provide useful insight into the molecular design of high-efficiency TADF emitters.



## 1. INTRODUCTION

Recently, the development of thermally activated delayed fluorescence (TADF) materials has become a research hot spot owing to the efficient upconversion of electro-pumped triplet states into singlet for organic light-emitting diodes (OLED).<sup>1–3</sup> In the electroluminescence device, electrons and holes are electrically injected from electrodes to form bound states (excitons) in the active layer, with statistically 25% singlet and 75% triplet excitons. Generally, for organic molecules only the singlet excitons fluoresce, rendering a limit of 25% for the internal quantum efficiency. TADF emitters can effectively convert the lowest triplet state ( $T_1$ ) into the lowest singlet state ( $S_1$ ) through reverse intersystem crossing (RISC) when the temperature rises, which largely improves the efficiency of exciton utilization and even makes it reach 100% in principle.<sup>4,5</sup> To obtain highly efficient TADF material, it is crucial to understand the ISC mechanism of the interconversion processes of  $T_1 \leftrightarrow S_1$ . Some efforts have been made to reveal the mechanism of RISC through experimental measurements and theoretical calculations.<sup>1–10</sup> Cyclic intersystem crossing was thought to mostly occur between charge-transfer single

(<sup>1</sup>CT) and triplet (<sup>3</sup>CT) states owing to significantly reduced energy gap.<sup>2,4</sup> Recently, it was suggested that RISC from <sup>3</sup>CT to <sup>1</sup>CT involves second order process with nonadiabatic coupling with the local exciton triplet (<sup>3</sup>LE) states as intermediate state which lies closer to <sup>1</sup>CT.<sup>7–10</sup> For instance, by using photoinduced absorption measurements combined with quantum dynamics simulations, Etherington et al. observed that the spin–orbit coupling between <sup>1</sup>CT and <sup>3</sup>CT is mediated by the lowest local exciton triplet (<sup>3</sup>LE) of donor in 2,8-di(10H-phenothiazin-10-yl)dibenzo[*b,d*]thiophene-5,5-dioxide.<sup>7,8</sup> Through quantum chemical calculations, Chen et al. obtained extremely small direct RISC rate constant for  $T_1 \rightarrow S_1$  under Fermi's golden rule and thus highlighted the important role of nonadiabatic transition at  $S_1-S_2$  and  $T_1-T_2$  conical intersection points in the potential energy surfaces (PESs) at the level of TDDFT/BMK/6-31G(d).<sup>9</sup> Marian proposed that an energetically close-lying LE state can mediate the triplet-to-

Received: January 22, 2017

Revised: May 22, 2017

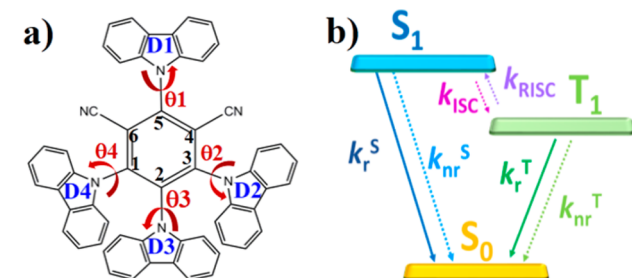
Published: May 30, 2017

singlet upconversion in ACRXTN based on the spin–orbit coupling constants and potential energy profiles calculated at the DFT/MRCI level.<sup>10</sup> These works demonstrated that the direct spin–orbit coupling between  $S_1$  and  $T_1$  is negligible or even forbidden and that the LE states close to  $T_1$  are important as an intermediate state for the second-order process for the donor–acceptor (DA)-type TADF emitters. In fact, the second-order process has been already proposed in a case study for anthracene by the authors.<sup>11</sup> The experimentally measured ISC rate value from  $S_1$  to  $T_2$  of anthracene can only be reproduced by adopting the ISC rate formalism based on the second-order perturbation theory combining nonadiabatic coupling and spin orbit coupling.<sup>11</sup>

In general, the radiative decay rates ( $\sim 10^{6-7} \text{ s}^{-1}$ ) of TADF emitters are smaller than those of traditional fluorophores of  $\sim 10^{8-9} \text{ s}^{-1}$ . Therefore, apart from effective RISC process, decreasing the nonradiative decay rate of  $S_1 \rightarrow S_0$  is also important for improving the quantum efficiency of TADF emitters. Thus, it is imperial to quantitatively predict the interconversion rate constants between the singlet and triplet states and the TADF quantum efficiency from first principles.

In this work, we chose a typical TADF emitter, 1,2,3,5-tetrakis(carbazol-9-yl)-4,6-dicyanobenzene (4CzIPN, see Scheme 1a) as an example because it has a wealth of

Scheme 1



L

<sup>a</sup>Chemical structure of 4CzIPN with key labels. <sup>b</sup>(b) Excited-state decay and conversion processes, including the fluorescent radiative ( $k_r^S$ ) and nonradiative internal conversion ( $k_{nr}^S$ ) from  $S_1$  to  $S_0$ , the intersystem crossing from  $S_1$  to  $T_1$  ( $k_{ISC}$ ), the reverse intersystem crossing from  $T_1$  to  $S_1$  ( $k_{RISC}$ ), and the fluorescent radiative ( $k_r^T$ ) and nonradiative intersystem crossing ( $k_{nr}^T$ ) from  $T_1$  to  $S_0$

photophysical and spectroscopic data in experiments. The interconversion and decay rate constants ( $k_r^S$ ,  $k_{nr}^S$ ,  $k_r^T$ ,  $k_{nr}^T$ ,  $k_{ISC}$ , and  $k_{RISC}$  in Scheme 1b) of  $S_1$  and  $T_1$  were quantitatively calculated using the thermal vibration correlation function (TVCF) rate formalism we developed earlier,<sup>11</sup> and the prompt and delayed fluorescence efficiencies were obtained correspondingly. It is found that an effective RISC from  $T_1$  to  $S_1$  occurs without the help of higher triplet and singlet states. The electronic-vibrational coupling analyses demonstrate that the pathways of interconversion between  $S_1$  and  $T_1$  is mainly ascribed as the free rotational motions of the carbazolyl group between two cyano groups, and the nonradiative dissipation channels are hampered by the large torsional barriers of other three adjacent carbazolyl groups, thus causing strong fluorescence. This work would provide design routes for high-performing TADF materials.

## 2. METHODOLOGY

**2.1. Optical Spectra.** On the basis of the Fermi's golden rule (FGR) and the Franck–Condon principle, the absorption spectrum  $\sigma_{ab}(\omega, T)$  and the emission spectrum  $\sigma_{em}(\omega, T)$  read<sup>12</sup>

$$\sigma_{ab}(\omega, T) = \frac{4\pi^2\omega}{3\hbar c} |\mu_{fi}|^2 \sum_{u,\nu} P_{iv} |\langle \Theta_{fu} | \Theta_{iv} \rangle|^2 \delta(\omega - \omega_{fu,iv}) \quad (1)$$

$$\sigma_{em}(\omega, T) = \frac{4\omega^3}{3\hbar c^3} |\mu_{fi}|^2 \sum_{u,\nu} P_{iv} |\langle \Theta_{fu} | \Theta_{iv} \rangle|^2 \delta(\omega_{iv,fu} - \omega) \quad (2)$$

Here  $P_{iv} = e^{-\beta \hat{H}} / Z_i$  represents the Boltzmann distribution function for the initial-state vibronic manifold at the finite temperature, in which  $Z_i = \text{Tr}(e^{-\beta \hat{H}})$  is the partition function;  $\Theta$  denotes the nuclear vibrational wave function;  $\nu$  and  $u$  are the vibrational quantum numbers of the initial and final states, respectively;  $\mu_{fi}$  is the electric transition dipole moment between the two electronic states  $|\Phi_i\rangle$  and  $|\Phi_f\rangle$ , which is independent of the nuclear coordinate under the Franck–Condon approximation.

Under the time-dependent TVCF formalism, eqs 1 and 2 can be recast into the time-dependent forms

$$\sigma_{abs}^{FC}(\omega, T) = \frac{2\pi\omega}{3\hbar c} |\mu_{fi}|^2 \int e^{i(\omega - \omega_{fi})t} \rho_{abs,0}^{FC}(t, T) dt \quad (3)$$

$$\sigma_{em}^{FC}(\omega, T) = \frac{2\omega^3}{3\pi\hbar c^3} |\mu_{fi}|^2 \int_{-\infty}^{\infty} e^{-i(\omega - \omega_{iv})t} \rho_{em,0}^{FC}(t, T) dt \quad (4)$$

The thermal vibration correlation functions (TVCFs)  $\rho_{abs,0}^{FC}(t, T)$  and  $\rho_{em,0}^{FC}(t, T)$  have the same form  $Z_i^{-1} \text{Tr}[e^{-i\tau_i \hat{H}_i} e^{-i\tau_f \hat{H}_i}]$  and can be solved analytically by multidimensional Gaussian integrations.<sup>13</sup> Here,  $\tau_i = -i\beta - t/\hbar$ ,  $\tau_f = t/\hbar$ ,  $\beta = (k_B T)^{-1}$  and  $\hat{H}_i$  ( $\hat{H}_f$ ) is the harmonic oscillator Hamiltonian of the final (initial) electronic state.

**2.2. Radiative and Nonradiative Decay Rate Constants.** The radiative decay rate constant is the integration over the whole emission spectrum

$$k_r(T) = \int \sigma_{em}(\omega, T) d\omega \quad (5)$$

According to the FGR and the second-order perturbation theory, the general nonradiative decay rate constant can be expressed as

$$k_{f \leftarrow i} = \frac{2\pi}{\hbar} \sum_{v,u} P_{iv} \left| H'_{fu,iv} + \sum_{n,\mu} \frac{H'_{fu,n\mu} H'_{n\mu,iv}}{E_{iv} - E_{n\mu}} \right|^2 \delta(E_{iv} - E_{fu}) \quad (6)$$

where  $H'$  denotes the interaction between two different Born–Oppenheimer states, consisting of two contributions as follows:

$$\hat{H}'\Psi_{iv} = \hat{H}^{BO} \Phi_i(\mathbf{r}; \mathbf{Q}) \Theta_v(\mathbf{Q}) + \hat{H}^{SO} \Phi_i(\mathbf{r}; \mathbf{Q}) \Theta_v(\mathbf{Q}) \quad (7)$$

Here  $\hat{H}^{BO}$  is the nonadiabatic coupling, and  $\hat{H}^{SO}$  is the spin–orbit coupling.

The intersystem crossing rate constant from initial singlet/triplet to triplet/singlet states can be recast based on the second-order perturbation theory as

$$k_{f \leftarrow i}^{\text{ISC}} = k_{f \leftarrow i}^{(0)} + k_{f \leftarrow i}^{(1)} + k_{f \leftarrow i}^{(2)} \quad (8)$$

where

$$k_{f \leftarrow i}^{(0)} \equiv \frac{1}{\hbar^2} |H_{fi}^{\text{SO}}|^2 \int_{-\infty}^{\infty} dt e^{i\omega_{if}t} \rho_{fi}^{(0)}(t) \quad (9)$$

$$k_{f \leftarrow i}^{(1)} \equiv \text{Re} \left[ \frac{2}{\hbar^2} \sum_k H_{fi}^{\text{SO}} T_{if,k} \int_{-\infty}^{\infty} dt e^{i\omega_{if}t} \rho_{fi,k}^{(1)}(t) \right] \quad (10)$$

$$k_{f \leftarrow i}^{(2)} \equiv \frac{1}{\hbar^2} \sum_{k,l} T_{if,k} T_{fi,l} \int_{-\infty}^{\infty} dt e^{i\omega_{if}t} \rho_{fi,kl}^{(2)}(t) \quad (11)$$

$T_{if,k(l)}$  is the mixed spin-orbit and nonradiative couplings between two electronic states for the  $k(l)$ th normal mode

$$T_{if,k(l)} = \sum_n (H_{in}^{\text{SO}} \langle \Phi_n | \hat{P}_{fk} | \Phi_i \rangle / \Delta E_{ni} + H_{ni}^{\text{SO}} \langle \Phi_i | \hat{P}_{nk} | \Phi_n \rangle / \Delta E_{in})$$

$\rho_{fi}^{(0)}(t)$  is the same as that in spectrum formula, and  $\rho_{fi,k}^{(1)}(t)$  and  $\rho_{fi,kl}^{(2)}(t)$  are  $Z_i^{-1} \text{Tr}[\hat{P}_{fk} e^{-i\tau_i \hat{H}_i} e^{-i\tau_l \hat{H}_l}]$  and  $Z_i^{-1} \text{Tr}[\hat{P}_{fk} e^{-i\tau_i \hat{H}_i} \hat{P}_{kl} e^{-i\tau_l \hat{H}_l}]$ , respectively.

The internal conversion rate constant between two electronic states with same spin manifold under can be written based on the first-order perturbation theory as<sup>14</sup>

$$k_{f \leftarrow i}^{\text{IC}} \equiv \frac{1}{\hbar^2} R_{kl} \int_{-\infty}^{\infty} dt e^{i\omega_{if}t} \rho_{fi}^{\text{ic}}(t, T) \quad (12)$$

where  $R_{fi,k} \equiv \langle \Phi_i | \hat{P}_{fk} | \Phi_i \rangle \langle \Phi_i | \hat{P}_{fi} | \Phi_i \rangle$  is the nonadiabatic electronic coupling matrix element.  $\rho_{fi}^{\text{ic}}(t, T)$  is the same as  $\rho_{fi,kl}^{(2)}(t)$  in eq 11. The detailed derivation and solution of equations can be found in our previous work.<sup>11,14,15</sup>

**2.3. Computational Details.** The geometry optimizations and frequency calculations were performed for the  $S_0$  and  $T_1$  states by density functional theory (DFT), and for the  $S_1$  state by time-dependent DFT (TDDFT). Six exchange-correlation functionals, namely, B3LYP, mPW1LYP, mPW1B95, BMK, M062X, and M06-HF with different HF exchange percentages in the XC functional of 20, 25, 31, 42, 54, and 100%, and two range-separated hybrid functionals, CAM-B3LYP and  $\omega$ B97XD, are used combining with the 6-31G(d) basis set. The solvent environments were mimicked by using the polarizable continuum model (PCM) with the equilibrium solvation applied for the geometry optimization and the nonequilibrium solvation for the single-point calculation at the equilibrium geometry.<sup>11,16</sup> All the calculations were carried out using the Gaussian 09 package.<sup>17</sup>

On the basis of the electronic properties, the radiative, internal conversion, and intersystem crossing rate constants were evaluated using the TVCF theory, as implemented in the MOMAP program package.<sup>11,15,16,18</sup> The potential energy surface (PES) of  $S_1$  was considered by using  $Q_{S_1} = Q_{S_0} + D$  or  $Q_{S_1} = Q_{T_1} + D$  relative to that of  $S_0$  or  $T_1$ , respectively. The vector  $D$  is the displacement between  $S_0$  and  $S_1$  or  $S_0$  and  $T_1$  geometries. Under the frame of the first-order perturbation theory, the nonadiabatic coupling was treated as the force acting on the atomic nuclei through the transition electric field at the level of TD/B3LYP/6-31G(d).<sup>14</sup> The transition electric field was evaluated by TDDFT using the Gaussian 09 package.

The spin-orbit coupling (SOC) matrix elements were treated as perturbation through state interaction,<sup>19</sup> and the SOC operator<sup>20</sup> results from the spin separation of the parent exact two-component Hamiltonian.<sup>21</sup> The SOC calculations were carried out at the TD/B3LYP/6-31G(d) level using the BDF program package.<sup>22</sup> The transition dipole moments from the  $T_1$  to  $S_0$  were computed from the quadratic response function using the Dalton program package.<sup>23,24</sup>

### 3. RESULTS AND DISCUSSION

**3.1. Geometric Structures.** It is still a challenging issue to choose a suitable exchange-correlation functional to accurately describe the excited-state properties of donor-acceptor-type molecules under the framework of TDDFT,<sup>25-29</sup> owing to the following reasons: spurious self-interaction,<sup>30</sup> missing derivative discontinuity,<sup>31,32</sup> adiabatic approximation in which the memory effects in time-dependent density evolution are neglected,<sup>33</sup> orbital relaxation energies and two-electron terms considered insufficiently in the linear response formalism,<sup>34</sup> and limitation of single-reference character.<sup>35</sup> Many efforts have been devoted to improving the description of electronic transition with charge-transfer (CT) character, including range-separated density functionals with individually tuned parameters<sup>36</sup> and optimal HF% in the XC functional under the framework of TDDFT,<sup>37</sup>  $\Delta$ SCF-DFT approach,<sup>38-40</sup> and multireference DFT method.<sup>35</sup> In addition, TDDFT encounters much difficulty in describing triplet excited states due to the triplet instabilities.<sup>41,42</sup> Recently, some benchmarks have been carried out to estimate the energy gap between the first excited singlet and triplet states for the TADF systems.<sup>43</sup> To the best of our knowledge, there does not exist any functional to well define both the first excited singlet and triplet states for CT molecules.

The molecular geometries in the  $S_0$ ,  $S_1$ , and  $T_1$  states of 4CzIPN in the gas phase were optimized using different density functionals. Figure 1 displays the frontier orbitals and excited-

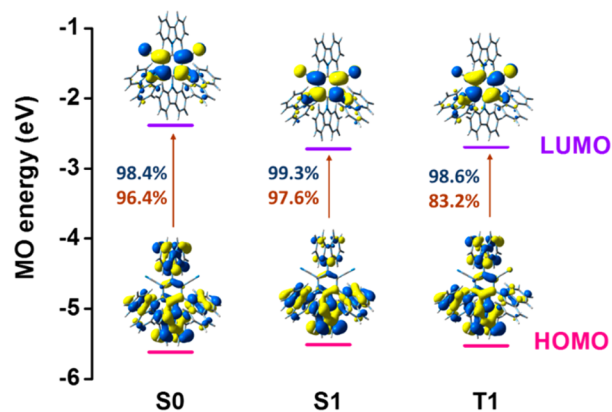


**Figure 1.** Frontier orbitals and transition proportion of HOMO  $\rightarrow$  LUMO for the  $S_1$  (blue number) and  $T_1$  (red number) states at the optimized  $S_0$ ,  $S_1$ , and  $T_1$  geometries for 4CzIPN in the gas phase.

state transition properties at the  $S_0$ ,  $S_1$ , and  $T_1$  geometries obtained at the B3LYP/6-31G(d) level. Obviously, the highest occupied molecular orbital (HOMO) is mainly localized on the carbazolyl groups while the lowest unoccupied molecular orbital (LUMO) is distributed on the dicyanobenzene moiety. Both the  $S_1$  and  $T_1$  transitions exhibit the feature of outstanding charge transfer (CT) from carbazolyl groups to dicyanobenzene

moiety and very minor local excitation (LE) on central phenyl ring at the optimized  $S_0$ ,  $S_1$ , and  $T_1$  geometries. It is also seen that the electronic density of HOMO becomes more localized to the three neighboring carbazolyl moieties in the optimized  $S_1$  state. This type of density localization is always relevant to bond twisting or termed as twist-induced intramolecular charge transfer (TICT). The torsional angles between the electron-donating and the electron-withdrawing moieties are expected to play a crucial role in determining the CT character. The calculated torsional angles between carbazolyl and dicyanobenzene moieties ( $\theta_1$ ,  $\theta_2$ ,  $\theta_3$ , and  $\theta_4$  in Scheme 1a) using different functionals, are presented in Figure 2 (detailed data

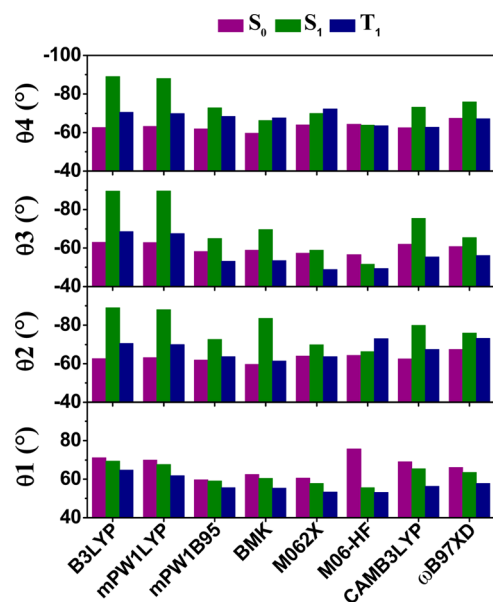


**Figure 2.** Density functional dependence of selected geometric parameters (dihedral angles) at the equilibrium geometries of the  $S_0$ ,  $S_1$ , and  $T_1$  states for 4CzIPN in the gas phase.

can be found in Table S1 of Electronic Supplementary Information (ESI)). It is easily seen that among the  $S_0$ ,  $S_1$ , and  $T_1$  states, the geometric structure of  $S_1$  is most sensitive to the choice of functionals. The predicted torsional angle increases with the decreasing HF fraction. For instance,  $\theta_3$  varies from about  $-51.6^\circ$  to  $-89.6^\circ$  with the decrease of the HF% in XC functional from 100% to 20%. The amount of charge transferred from donor to acceptor are calculated and given in Table S2 of ESI. As expected, the amount of CT is more pronounced with large torsional angles, as observed in many previous systems such as benzylidene malononitrile.<sup>44</sup>

These indicate that the amount of CT is sensitive to the choice of xc-functional.

The geometric modifications between  $S_1$  and  $S_0$  play an important role in the photophysical properties because they can largely control the optical spectrum shape and the nonradiative decay rate based on the Franck–Condon principle.<sup>45</sup> Table 1 lists the modifications of the key torsional angles and bond lengths from  $S_1$  to  $S_0$  states at different computational levels. The changes of torsional angles are very susceptible to functionals, and there is not a monotonous variation as a function of the HF fraction in XC functional. B3LYP and mPW1LYP with the smallest HF% give the largest change of ca.  $80^\circ$ . The M062X functional with 54% HF fraction gives the smallest modification of  $16^\circ$ . And the other density functionals show a moderate change of  $24^\circ \sim 45^\circ$ . These results suggest that the computed photophysical properties would be diverse by using different density functionals. In addition, the largest modifications of bond lengths appear in the carbon–carbon bonds in the central phenyl ring and they are insensitive to density functional. The molecular geometries at the three states were also optimized in toluene at the M062X level, which are almost identical to those in the gas phase (see Table S3 of ESI). This indicates that nonpolar solvent would hardly affect the molecular geometry. By and large, it is of vital importance to choose a suitable functional according to a certain criterion.

Stokes shift between the absorption and emission spectra is usually used to assess the performance of an approach to calculate the lowest singlet excited state. Stokes shift is approximately equal to the total geometric reorganization energy at  $S_1$  and  $S_0$  potential energy surfaces in harmonic oscillator model.<sup>46</sup> Thus, large reorganization energy would lead to remarkable Stokes shift and *vice versa*. Table 1 presents the total reorganization energy ( $\lambda_{\text{reorg}}$ ) at the ground-state potential energy surface at different density functional levels. The contribution of each normal mode to the reorganization energy is given in Figure S1 of ESI. Here the reorganization energy of the  $i$ th normal mode ( $\lambda_i$ ) is calculated by  $\lambda_i = S_i \hbar \omega_i = \omega_i^2 \Delta D_i^{2/2}$  ( $S_i$  and  $\omega_i$  represent the Huang–Rhys factor and frequency of the  $i$ th normal mode, and  $\Delta D_i$  is the displacement along the  $i$ th normal mode coordinate between the equilibrium geometries of two electronic states). As expected, the change trend of  $\lambda_{\text{reorg}}$  is very similar to the geometric structure modification. The reorganization energy given by M062X is the smallest and the main contributions come from a low-frequency torsional vibration of  $35 \text{ cm}^{-1}$  and a high-frequency carbon–carbon stretching vibration of  $1627 \text{ cm}^{-1}$ . M062X functional predicts the smallest Stokes shift ( $\nu = 2\lambda_{\text{reorg}}$ ) of  $0.56 \text{ eV}$  ( $0.54 \text{ eV}$  in toluene), closest to the experimental value of  $0.30 \text{ eV}$ .<sup>2</sup> Table 2 gives the absorption and emission energies (vertical

**Table 1.** Modifications of the Key Torsional Angles (deg) and Bond Lengths (Å) and the Reorganization Energy ( $\lambda_{\text{reorg}}$ , eV) for the Transition from  $S_1$  to  $S_0$  Obtained at Different Density Functional Levels for 4CzIPN

	HF%	$\Delta\theta_1$	$\Delta\theta_2$	$\Delta\theta_3$	$\Delta\theta_4$	$\Sigma \Delta\theta $	$L_{\text{C1-C6}}$	$L_{\text{C3-C4}}$	$\lambda_{\text{reorg}}$
B3LYP	20%	-1.8	-26.4	-26.6	-26.4	81.2	0.044	0.044	0.98
mPW1LYP	25%	-2.3	-24.8	-26.8	-24.8	78.7	0.046	0.046	1.05
mPW1B95	31%	-0.2	-10.8	-6.8	-11.0	28.8	0.040	0.040	0.45
BMK	42%	-1.9	-23.8	-10.7	-6.6	43.0	0.047	0.044	0.75
M062X	54%	-2.8	-5.8	-1.6	-5.9	16.1	0.040	0.040	0.28
M06-HF	100%	-5.9	-20.0	-16.9	-20.0	62.8	0.045	0.045	1.14
CAMB3LYP		-3.7	-17.4	-13.3	-10.7	45.1	0.041	0.041	0.31
$\omega$ B97XD		-2.6	-8.5	-4.6	-8.5	24.2	0.042	0.042	0.32

**Table 2. Vertical Energy (eV) at the  $S_0$  and  $S_1$  Minimum and the Emissive Oscillator Strength at Different Density Functional Levels**

	$\Delta E_v(S_{0min})$	$\Delta E_v(S_{1min})$	Stoke shifts	oscillator strengths
B3LYP	2.49	1.70	0.79	$1.67 \times 10^{-5}$
mPW1LYP	2.66	1.88	0.78	$6.68 \times 10^{-5}$
mPW1B95	2.86	2.28	0.58	0.037
BMK	3.09	2.41	0.68	0.024
M062X	3.35	2.94	0.41	0.087
M06-HF	4.03	2.06	1.97	0.011
CAMB3LYP	3.36	2.76	0.60	0.024
$\omega$ B97XD	3.46	2.98	0.48	0.062
exp. (ref 2)	2.76	2.45	0.30	

excitation energy), and the emissive oscillator strengths, obtained with the different functionals, as well as available experimental values. As expected, M062X give the largest oscillator strength and the smallest Stokes shift due to the smallest distorted angles at  $S_1$  minimum and the smallest geometrical modification from  $S_1$  to  $S_0$ , which are in accordance with the experimentally observed strong fluorescence.<sup>2</sup> However, the excited state energies obtained by M062X are much larger than the measured values. The calculated oscillator strengths by B3LYP and mPW1LYP are negligibly small, which is not in accordance with the observed fluorescence. The results from other functionals fall between the two cases. To conclude, the M062X-optimized geometries appear to be most reasonable to estimate the ground-state and excited-state geometries of 4CzIPN.

**3.2. Excited-State Energies.** RISC depends on the energy gap between  $S_1$  and  $T_1$  ( $\Delta E_{ST}$ ), which is calculated by the M062X functional to be 0.35 and 0.32 eV in the gas phase and toluene solvent, respectively, far larger than the experimental value. Thus, it is necessary to further assess the capabilities of different density functionals to predict the excited-state energies based on the M062X-derived ground-state and excited-state geometries (see Table S4 of ESI). The activation energy is a key factor to control RISC from  $T_1$  to  $S_1$ , and it is reasonable to use it as a criterion parameter to evaluate the performance of density functionals in defining both  $S_1$  and  $T_1$ . In experiments, the activation energy could be estimated from the Arrhenius formula  $k_{RISC} = A \exp(-\Delta G_a/k_B T)$  in combination with the RISC rates measured at different temperatures. Actually, the Arrhenius formula can be derived from the full-quantum rate formula eq 9 by adopting the short-time and high-temperature

approximations (see detailed derivation in ESI), and the activation energy is hence obtained as  $\Delta G_a = (-\Delta E_{if} + \lambda_{reorg})^2 / (4\lambda_{reorg})$ . Herein,  $\Delta E_{if} = E_i - E_f$  denotes the adiabatic energy difference between the initial  $T_1$  and final  $S_1$  states.  $\lambda_{reorg}$  represents the reorganization energy at the potential energy surface of the  $S_1$  state, which could be calculated by using two-point method based on the excitation energy, namely,  $\lambda_{reorg} = E_{S_1}(T_1, \text{geometry}) - E_{S_1}(S_1, \text{geometry})$  [ $E_{S_1}(T_1/S_1, \text{geometry})$  is the  $S_1$  energy at the  $T_1/S_1$  equilibrium geometry]. Figure 3 plots the results of  $\Delta E_{ST}$ ,  $\lambda_{reorg}$  and  $\Delta G_a$  obtained by different density functionals at the M062X-optimized geometry. The corresponding dependence of  $\Delta E_{ST}$  and  $\lambda_{reorg}$  on the HF fraction in the XC functionals is plotted in Figures S2 and S3 of ESI, respectively. The  $\Delta E_{ST}$  and  $\Delta G_a$  increases with the HF fraction in the XC functional while the  $\lambda_{reorg}$  decreases. Because of the overestimation of  $\Delta E_{ST}$  and extremely small  $\lambda_{reorg}$ , the  $\Delta G_a$  is largely overestimated by M06-HF. The LRC functionals CAMB3LYP and  $\omega$ B97XD give an unreasonable  $\Delta G_a$  owing to a too large  $\Delta E_{ST}$  of ca. 0.6 eV. Compared with the experiments, B3LYP offers the best result of 0.092 eV, in very good agreement with the measured values of 0.084 eV in toluene and 0.1 eV in thin film.<sup>2</sup> Therefore, the B3LYP-calculated excitation energies seem to be most reliable and they would be used for the following rate constant calculations.

**3.3. Interconversion Rates and Fluorescence Efficiencies.** We first searched the minimal energy path (MEP) of  $S_1$  state starting from  $T_1$  to  $S_1$  equilibrium geometries at level of TD-M062X/6-31G(d) and calculated the potential surfaces of the  $S_1$ ,  $T_1$  and  $T_2$  states along the MEP by using both M06-2X and B3LYP functionals (see section VIII and Figure S4 in ESI). It is found that  $S_1$  is always above  $T_1$  and below  $T_2$  at the level of the hybrid TD-M062X/B3LYP, and  $T_2$  is not considered in the following rate calculations for TADF processes. The calculated average spin-orbit coupling value between  $S_1$  and  $T_1$  is 0.18  $\text{cm}^{-1}$ , which can induce the occurrence of ISC if the energy gap is small enough. Therefore, the thermal vibration correlation function rate formula in the framework of the first-order perturbation theory can be used to evaluate the interconversion rate constants among the  $S_1$ ,  $T_1$  and  $S_0$  states. Based on the geometric/electronic properties obtained by the hybrid M062X/B3LYP approach, the calculated rate constants are given in Figure 4a (detailed data seen in Table S5 of ESI), as well as the prompt and delayed fluorescent efficiencies. The displacement and torsion effects of all the normal vibration modes were considered, and the solvent effect was not taken

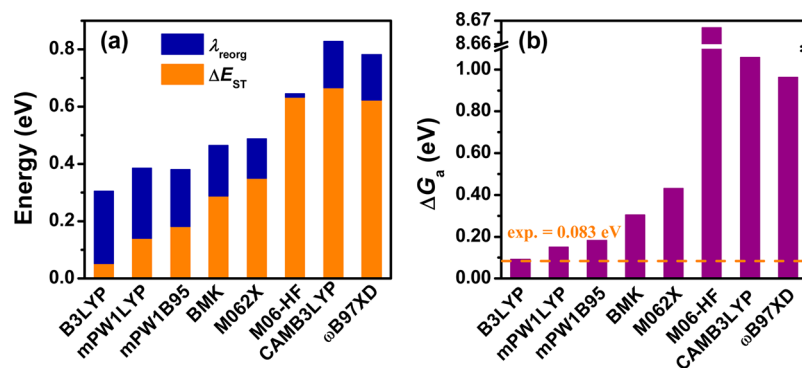


**Figure 3.** (a) Adiabatic energy differences ( $\Delta E_{ST}$ ) and reorganization energy ( $\lambda_{reorg}$ ); (b) activation energies ( $\Delta G_a$ , the dashed horizontal line denotes the experimental value) of the RISC from  $T_1$  to  $S_1$  calculated using different density functionals based on the M062X-optimized geometries for 4CzIPN.

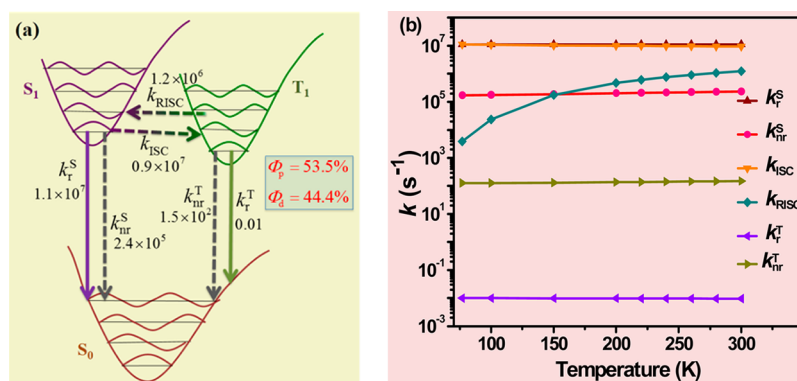


**Figure 4.** (a) The calculated conversion and decay rates (in unit of s<sup>-1</sup>) of S<sub>1</sub> and T<sub>1</sub> states and the prompt and delayed fluorescence quantum efficiency ( $\Phi_p = \frac{k_r^S}{k_r^S + k_{nr}^S + k_{ISC}}$  and  $\Phi_d = \sum_{m=1}^{\infty} (\Phi_{ISC} \Phi_{RISC})^m \Phi_p$  with  $\Phi_{ISC} = \frac{k_{ISC}}{k_r^S + k_{nr}^S + k_{ISC}}$  and  $\Phi_{RISC} = \frac{k_{RISC}}{k_r^T + k_{nr}^T + k_{RISC}}$ ) at 300 K and (b) the temperature dependence of the interconversion and decay rates from 77 to 300 K for 4CzIPN.

into account because of the hardly influence on molecular electronic structure property as tested above. In order to check how much the calculated rates depend on the choice of the method, we provided the calculated rates using the same functional (M062X and B3LYP) for geometries and energies for comparison in Table S6 of ESI. Since the singlet–triplet energy gap from M062X is too large, the rate constant of RISC is 6 orders of magnitude smaller than the experiment. The radiative rate constant with B3LYP is 4 orders of magnitude less than the experiment because of tiny oscillator strength and the nonradiative decay rate for S<sub>1</sub> → S<sub>0</sub> is 2 orders of magnitude larger than the experiment because of the overlarge geometrical modification. The hybrid approach of M062X for nuclear and B3LYP for electronic properties is suitable for the DA-type molecule. Strikingly, the RISC rate constant of T<sub>1</sub> → S<sub>1</sub> is calculated to be  $1.23 \times 10^6$  s<sup>-1</sup> based on the first-order perturbation which is very close to the experimental data of  $2.70 \times 10^6$  s<sup>-1</sup>.

The temperature dependence of the interconversion rate constants was examined and shown in Figure 4b (detailed data seen in Table S5 of ESI). The activation energy is fit to be 0.051 eV using the Arrhenius formula on the basis of the calculated RISC rate constants in Figure S5 of ESI, which is very closed to the experimental value and smaller than the value computed from the classical model given in section 3.2. This indicates that the present calculated result is reliable and that the quantum tunneling effect slightly facilitates the occurrence of RISC from T<sub>1</sub> to S<sub>1</sub>. As seen in Figure 4b,  $k_r^S$  hardly changes with temperature, as expected.<sup>45</sup> The value of  $k_{nr}^S$  increases with temperature owing to the participation of more vibrational states. The values of  $k_r^T$  and  $k_{nr}^T$  are expected to be very small due to weak spin–orbit couplings and large energy gap, which would facilitate the reverse conversion from T<sub>1</sub> to S<sub>1</sub> owing to thermal equilibrium. More interestingly, the  $k_{RISC}$  is substantially increased by 3 orders of magnitude while  $k_{ISC}$  is almost unchanged when temperature rises from 77 to 300 K. At 300 K, the RISC rate can compete with the other rates. Thus, the delayed fluorescence emerges. The resultant prompt and delayed fluorescence quantum efficiencies are 53.5 and 44.4%, respectively, at 300 K, and the total photoluminescent efficiency is 97.9%, which is very close to the experimental value of  $94 \pm 2\%$  measured in toluene.<sup>2</sup>

In order to gain a deep insight into the different behaviors of  $k_{ISC}$  and  $k_{RISC}$ , we plot  $k_{ISC}$  and  $k_{RISC}$  as a function of the energy

gap at different temperatures in Figure 5. When the energy gap is equal to  $\Delta E_{ST}$  or  $\Delta E_{TS}$ , the rate corresponds to  $k_{ISC}$  or  $k_{RISC}$ .

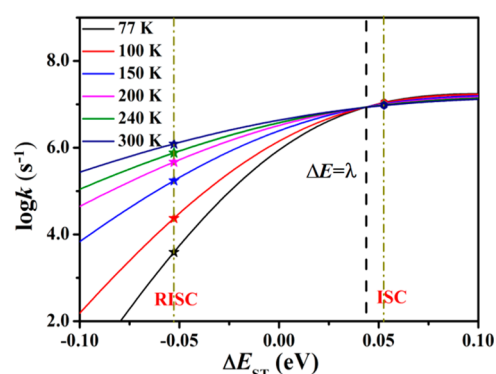


**Figure 5.** Intersystem crossing rate constant as a function of energy gap at different temperatures of 4CzIPN. The points marked with solid stars and circles represent  $k_{RISC}$  and  $k_{ISC}$ , respectively, and the black dotted line is the  $\Delta E = \lambda$ .

and the function can be approximated as a parabola of  $\ln(k) = \text{constant} - \frac{(-\Delta E + \lambda)^2}{4\lambda k_B T}$  based on linearly displaced model and short-time approximation. When  $\Delta E = \lambda$ , the rate is almost temperature-independent, and the temperature effect would appear until far away from the point of  $\Delta E = \lambda$ . Thus, RISC rate is more sensitive to temperature than ISC rate. It is easier to understand the phenomena from the point of view of energy conservation. Assuming temperature is 0 K, the transition starts from the lowest vibration state of the initial electronic state to a higher vibration state of the final electronic state. For ISC, the energy conservation is naturally favorable to a higher vibration state of T<sub>1</sub> state owing to  $\Delta E_{ST} > 0$ . However, for RISC, the energy conservation cannot be satisfied because of  $\Delta E_{TS} < 0$ . Only when the temperature rises to a certain value, the energy conservation is achieved; hence, the RISC can occur. Therefore, RISC rate is more suspicious to temperature than ISC rate.

To figure out the structure–property relationship during the energy conversion processes of S<sub>1</sub> ↔ T<sub>1</sub> and S<sub>1</sub> → S<sub>0</sub>, we analyzed the Huang–Rhys factors as well as the displacement vectors of vibration modes with the largest Huang–Rhys factors (see Figure 6). For the conversion between S<sub>1</sub> and T<sub>1</sub>,

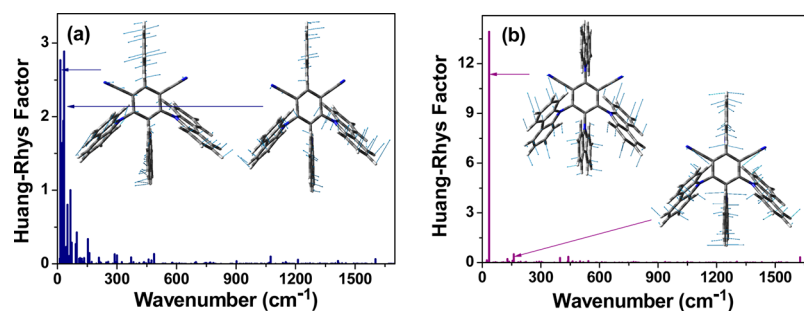


**Figure 6.** Huang–Rhys factors for energy conversion between  $S_1$  and  $T_1$  (a) and between  $S_1$  and  $S_0$  (b), as well as the displacement vectors of two important vibration modes with the largest values of Huang–Rhys factor for 4CzIPN.

many low-frequency vibration modes ( $<100\text{ cm}^{-1}$ ) have significant Huang–Rhys factors which correspond to the rotation motion of the carbazolyl groups. Herein, the two modes with the largest Huang–Rhys factors are assigned to the torsional motion of four carbazolyl groups (D1, D2, D3, and D4) and of a single carbazolyl group D1, respectively. This suggests that the free rotation of carbazolyl D1 can provide an important channel to energy conversion between  $S_1$  and  $T_1$ . In contrast, for the decay process from  $S_1$  to  $S_0$ , only a single vibration mode exhibits an extraordinarily huge Huang–Rhys factor, and it is related to the torsional motion of the three adjacent carbazolyls (D2, D3, and D4). This indicates that the rotation of the three adjacent carbazolyls plays a main role in determining the nonradiative decay rate of  $S_1 \rightarrow S_0$ , their large torsional barriers are sure to restrict the nonradiative decay to large extent owing to significant steric hindrance.

#### 4. CONCLUSIONS

We have comprehensively investigated the electronic structures and photophysical properties of 4CzIPN by combining first-principle calculations and our thermal vibration correlation function rate theory. Comparing the calculated absorption and emission spectra, Stokes shift, and the activation energy of  $T_1 \rightarrow S_1$  with experimental counterparts, the hybrid M062X/B3LYP is found to be the most suitable computational scheme. The conversion and decay rate constants of  $S_1$  and  $T_1$  states, including the radiative and nonradiative rate constants of  $S_1$  and  $T_1$  and the ISC and RISC rates of  $S_1 \leftrightarrow T_1$ , have been computed at different temperature by using the thermal vibration correlation function rate formula based on first-order perturbation rate theory. The RISC rate constant is sharply speeding up whereas the other decay rates are hardly or slightly changed with temperature increasing. At 300 K, the RISC rate of  $1.23 \times 10^6\text{ s}^{-1}$  appear to be comparable to the radiative decay rate of  $1.11 \times 10^7\text{ s}^{-1}$  and the nonradiative rate of  $2.37 \times 10^5\text{ s}^{-1}$  of  $S_1$ , rendering effective conversion from  $T_1$  to  $S_1$  and occurrence of the TADF phenomenon. Hence, the electronic-vibrational coupling activated by temperature is responsible for the occurrence of delayed fluorescence in 4CzIPN. It is noteworthy that the effective RISC occurs directly between  $T_1$  and  $S_1$  and does not need the help of intermediate triplet or singlet states in higher energy. More strikingly, it is learned that the relatively free rotational motions of the isolated carbazolyl group between two cyano groups offer effective pathways for the conversion of  $S_1 \leftrightarrow T_1$ , and the large torsional barriers of other three adjacent carbazolyl groups make 4CzIPN quite rigid upon excitation and restrict the nonradiative energy dissipation, which results in strong prompt and delayed fluorescence. These provide the ideas to open a channel of  $S_1$

$\leftrightarrow T_1$  by a freely motional moiety and blocked the nonradiative pathway of  $S_1 \rightarrow S_0$  by some compactly inflexible moieties, which would be helpful for designing novel for excellent TADF materials. Along this line, further studies on many other TADF molecular materials are ongoing in our group.

#### ■ ASSOCIATED CONTENT

##### Supporting Information

The Supporting Information is available free of charge on the ACS Publications website at DOI: 10.1021/acs.jpcc.7b00692.

Torsion angles for the molecular geometries optimized and the reorganization energies obtained; vertical and adiabatic excitation energies and the energy differences between the  $S_1$  and  $T_1$  states and reorganization energies between  $S_1$  and  $T_1$  on the HF fraction; derivation of activation energy equation under the framework of short-time and high-temperature approximations; potential energy surfaces of the  $S_1$ ,  $T_1$  and  $T_2$  states; vibronic coupling-induced interconversion rate constants at different temperatures; and the linear fitting of  $\ln(k_{\text{RISC}}) \propto 1/T$  (PDF)

#### ■ AUTHOR INFORMATION

##### Corresponding Authors

\*E-mail: [yypyi@iccas.ac.cn](mailto:yypyi@iccas.ac.cn)

\*E-mail: [zgshuai@tsinghua.edu.cn](mailto:zgshuai@tsinghua.edu.cn)

##### ORCID

Qian Peng: 0000-0001-8975-8413

Yuanping Yi: 0000-0002-0052-9364

Zhigang Shuai: 0000-0003-3867-2331

##### Notes

The authors declare no competing financial interest.

#### ■ ACKNOWLEDGMENTS

The work is supported by the National Natural Science Foundation of China (Grants 21473214, 21290191, and 91233105), the Ministry of Science and Technology of China through the 973 program (Grants 2015CB65502, 2013CB834703, and 2013CB933503), and the Strategic Priority Research Program of the Chinese Academy of Sciences (Grant XDB12020200). We gratefully thank Dr. Zhendong Li, Dr. Bingbing Suo, and Wenjian Liu for providing the help in using BDF for the calculation of spin–orbit coupling matrix elements and Dr. Lili Lin for discussion about geometry optimization.

## REFERENCES

- (1) Hirata, S.; Sakai, Y.; Masui, K.; Tanaka, H.; Lee, S. Y.; Nomura, H.; Nakamura, N.; Yasumatsu, M.; Nakanotani, H.; Zhang, Q.; Shizu, K.; Miyazaki, H.; Adachi, C. Highly Efficient Blue Electroluminescence Based on Thermally Activated Delayed Fluorescence. *Nat. Mater.* **2014**, *14*, 330–336.
- (2) Uoyama, H.; Goushi, K.; Shizu, K.; Nomura, H.; Adachi, C. Highly efficient organic light-emitting diodes from delayed fluorescence. *Nature* **2012**, *492*, 234–238.
- (3) Tao, Y.; Yuan, K.; Chen, T.; Xu, P.; Li, H. H.; Chen, R. F.; Zheng, C.; Zhang, L.; Huang, W. Thermally Activated Delayed Fluorescence Materials Towards the Breakthrough of Organoelectronics. *Adv. Mater.* **2014**, *26*, 7931–7958.
- (4) Zhang, Q.; Li, B.; Huang, S.; Nomura, H.; Tanaka, H.; Adachi, C. Efficient Blue Organic Light-Emitting Diodes Employing Thermally Activated Delayed Fluorescence. *Nat. Photonics* **2014**, *8*, 326–332.
- (5) Adachi, C. Third-generation organic electroluminescence materials. *Jpn. J. Appl. Phys.* **2014**, *53*, 060101.
- (6) Ogiwara, T.; Wakikawa, Y.; Ikoma, T. Mechanism of Intersystem Crossing of Thermally Activated Delayed Fluorescence Molecules. *J. Phys. Chem. A* **2015**, *119*, 3415–3418.
- (7) Etherington, M. K.; Gibson, J.; Higginbotham, H. F.; Penfold, T. J.; Monkman, A. P. Revealing the spin–vibronic coupling mechanism of thermally activated delayed fluorescence. *Nat. Commun.* **2016**, *7*, 13680.
- (8) Gibson, J.; Monkman, A. P.; Penfold, T. J. The importance of vibronic coupling for efficient reverse intersystem crossing in thermally activated delayed fluorescence molecules. *ChemPhysChem* **2016**, *17*, 2956–2961.
- (9) Chen, X.; Zhang, S.; Fan, J.; Ren, A. Nature of highly efficient thermally activated delayed fluorescence in organic light-emitting diode emitters: nonadiabatic effect between excited states. *J. Phys. Chem. C* **2015**, *119*, 9728–9733.
- (10) Marian, C. M. Mechanism of the triplet-to-singlet upconversion in the assistant dopant ACRXTN. *J. Phys. Chem. C* **2016**, *120*, 3715–3721.
- (11) Peng, Q.; Niu, Y. L.; Shi, Q.; Gao, X.; Shuai, Z. G. Correlation Function Formalism for Triplet Excited State Decay: Combined Spin–Orbit and Nonadiabatic Couplings. *J. Chem. Theory Comput.* **2013**, *9*, 1132–1143.
- (12) Lin, S. H.; Chang, C. H.; Liang, K. K.; Chang, R.; Shiu, Y. J.; Zhang, J. M.; Yang, T. S.; Hayashi, M.; Hsu, F. C. Ultrafast dynamics and spectroscopy of bacterial photosynthetic reaction centers. *Adv. Chem. Phys.* **2002**, *121*, 1–88.
- (13) Ianconescu, R.; Pollak, E. Photoinduced Cooling of Polyatomic Molecules in an Electronically Excited State in the Presence of Dushinskii Rotations. *J. Phys. Chem. A* **2004**, *108*, 7778–7784.
- (14) Peng, Q.; Yi, Y.; Shuai, Z. G.; Shao, J. S. Excited state radiationless decay process with Duschinsky rotation effect: Formalism and implementation. *J. Chem. Phys.* **2007**, *126*, 114302.
- (15) Niu, Y. L.; Peng, Q.; Deng, C. M.; Gao, X.; Shuai, Z. G. Theory of Excited State Decays and Optical Spectra: Application to Polyatomic Molecules. *J. Phys. Chem. A* **2010**, *114*, 7817–7831.
- (16) (a) Tomasi, J.; Mennucci, B.; Cammi, R. Quantum Mechanical Continuum Solvation Models. *Chem. Rev.* **2005**, *105*, 2999. (b) Improta, R. UV–Visible Absorption and Emission Energies in Condensed Phase by PCM-TD-DFT Methods. In *Computational Strategies for Spectroscopy: From Small Molecules to Nanosystems*; Barone, V., Ed.; John Wiley & Sons: Chichester, U.K., 2011; pp 39–76. (c) Scalmani, G.; Frisch, M. J.; Mennucci, B.; Tomasi, J.; Cammi, R.; Barone, V. *J. Chem. Phys.* **2006**, *124*, 094107.
- (17) Frisch, M. J.; Trucks, G. W.; Schlegel, H. B.; Scuseria, G. E.; Robb, M. A.; Cheeseman, J. R.; Scalmani, G.; Barone, V.; Mennucci, B.; Petersson, G. A.; Nakatsuji, H.; Caricato, M.; Li, X.; Hratchian, H. P.; Izmaylov, A. F.; Bloino, J.; Zheng, G.; Sonnenberg, J. L.; Hada, M.; Ehara, M.; Toyota, K.; Fukuda, R.; Hasegawa, J.; Ishida, M.; Nakajima, T.; Honda, Y.; Kitao, O.; Nakai, H.; Vreven, T.; Montgomery, J. A., Jr.; Peralta, J. E.; Ogliaro, F.; Bearpark, M.; Heyd, J. J.; Brothers, E.; Kudin, K. N.; Staroverov, V. N.; Kobayashi, R.; Normand, J.; Raghavachari, K.; Rendell, A.; Burant, J. C.; Iyengar, S. S.; Tomasi, J.; Cossi, M.; Rega, N.; Millam, J. M.; Klene, M.; Knox, J. E.; Cross, J. B.; Bakken, V.; Adamo, C.; Jaramillo, J.; Gomperts, R.; Stratmann, R. E.; Yazyev, O.; Austin, A. J.; Cammi, R.; Pomelli, C.; Ochterski, J. W.; Martin, R. L.; Morokuma, K.; Zakrzewski, V. G.; Voth, G. A.; Salvador, P.; Dannenberg, J. J.; Dapprich, S.; Daniels, A. D.; Farkas, O.; Foresman, J. B.; Ortiz, J. V.; Cioslowski, J.; Fox, D. J. *Gaussian 09*, revision D.01; Gaussian, Inc.: Wallingford, CT, 2009.
- (18) Shuai, Z. G.; Peng, Q.; Niu, Y. L.; Geng, H. *MOMAP, a molecular materials property prediction package*, revision 0.2.004; Tsinghua University: Beijing, China, 2014. <http://www.shuaigroup.net/>.
- (19) Li, Z.; Suo, B.; Zhang, Y.; Xiao, Y.; Liu, W. Combining spin-adapted open-shell TD-DFT with spin-orbit coupling. *Mol. Phys.* **2013**, *111*, 3741–3755.
- (20) (a) Li, Z.; Xiao, Y.; Liu, W. On the spin separation of algebraic two-component relativistic Hamiltonians. *J. Chem. Phys.* **2012**, *137*, 154114. (b) Li, Z.; Xiao, Y.; Liu, W. *J. Chem. Phys.* **2014**, *141*, 054111.
- (21) Liu, W. J. Ideas of relativistic quantum chemistry. *Mol. Phys.* **2010**, *108*, 1679–1706.
- (22) Liu, W. J.; Hong, G. Y.; Dai, D. D.; Li, L. M.; Dolg, M. The Beijing four-component density functional program package (BDF) and its application to EuO, EuS, YbO and YbS. *Theor. Chem. Acc.* **1997**, *96*, 75–83. (b) Liu, W. J.; Wang, F.; Li, L. M. The Beijing Density Functional (BDF) Program Package: Methodologies and Applications. *J. Theor. Comput. Chem.* **2003**, *2*, 257–272. (c) Liu, W. J.; Wang, F.; Li, L. M. Relativistic Density Functional Theory: The BDF Program Package. *Recent Adv. Comput. Chem.* **2004**, *5*, 257.
- (23) Minaev, B.; Agren, H. Theoretical DFT study of phosphorescence from porphyrins. *Chem. Phys.* **2005**, *315*, 215–239.
- (24) *Dalton, a molecular electronic structure program*, release Dalton2011. <http://daltonprogram.org>.
- (25) Kümmel, S.; Kronik, L. Orbital-dependent density functionals: Theory and applications. *Rev. Mod. Phys.* **2008**, *80*, 3–60.
- (26) Cohen, A. J.; Mori-Sánchez, P.; Yang, W. Insights into Current Limitations of Density Functional Theory. *Science* **2008**, *321*, 792–794.
- (27) (a) Casida, M. E.; Huix-Rotllant, M. Progress in Time-Dependent Density-Functional Theory. *Annu. Rev. Phys. Chem.* **2012**, *63*, 287–323. (b) Adamo, C.; Jacquemin, D. The calculations of excited-state properties with Time-Dependent Density Functional Theory. *Chem. Soc. Rev.* **2013**, *42*, 845–856.
- (28) Shuai, Z. G.; Liu, W. J.; Liang, W. Z.; Shi, Q.; Chen, H. Theoretical Study of the Low-Lying Electronic Excited States for Molecular Aggregates. *Sci. China: Chem.* **2013**, *56*, 1258–1262.
- (29) Baer, R.; Livshits, E.; Salzner, U. Tuned Range-Separated Hybrids in Density Functional Theory. *Annu. Rev. Phys. Chem.* **2010**, *61*, 85–109.
- (30) Dreuw, A.; Head-Gordon, M. Failure of Time-Dependent Density Functional Theory for Long-Range Charge-Transfer Excited States: The Zincbacteriochlorin–Bacteriochlorin and Bacteriochlorophyll–Spheroidene Complexes. *J. Am. Chem. Soc.* **2004**, *126*, 4007–4016.
- (31) Tozer, D. J. Relationship between long-range charge-transfer excitation energy error and integer discontinuity in Kohn–Sham theory. *J. Chem. Phys.* **2003**, *119*, 12697–12699.
- (32) Peach, M. J. G.; Benfield, P.; Helgaker, T.; Tozer, D. J. Excitation energies in density functional theory: An evaluation and a diagnostic test. *J. Chem. Phys.* **2008**, *128*, 044118.
- (33) Maitra, N. T.; Burke, K.; Woodward, C. Memory in Time-Dependent Density Functional Theory. *Phys. Rev. Lett.* **2002**, *89*, 023002.
- (34) Kawasaki, T.; Kim, K.; Onuki, A. Dynamics in a tetrahedral network glassformer: Vibrations, network rearrangements, and diffusion. *J. Chem. Phys.* **2014**, *140*, 184502.
- (35) Filatov, M. Description of electron transfer in the ground and excited states of organic donor–acceptor systems by single-reference and multi-reference density functional methods. *J. Chem. Phys.* **2014**, *141*, 124123.

(36) Stein, T.; Kronik, L.; Baer, R. Reliable prediction of charge transfer excitations in molecular complexes using time-dependent density functional theory. *J. Am. Chem. Soc.* **2009**, *131*, 2818–2820.

(37) Huang, S.; Zhang, Q.; Shiota, Y.; Nakagawa, T.; Kuwabara, K.; Yoshizawa, K.; Adachi, C. Computational Prediction for Singlet- and Triplet-Transition Energies of Charge-Transfer Compounds. *J. Chem. Theory Comput.* **2013**, *9*, 3872–3877.

(38) Zhekova, H. R.; Seth, M.; Ziegler, T. A perspective on the relative merits of time-dependent and time-independent density functional theory in studies of the electron spectra due to transition metal complexes. An illustration through applications to copper tetrachloride and plastocyanin. *Int. J. Quantum Chem.* **2014**, *114*, 1019–1029.

(39) Ziegler, T.; Seth, M.; Krykunov, M.; Autschbach, J. A revised electronic Hessian for approximate time-dependent density functional theory. *J. Chem. Phys.* **2008**, *129*, 184114.

(40) Gilbert, A. T. B.; Besley, N. A.; Gill, P. M. W. Self-Consistent Field Calculations of Excited States Using the Maximum Overlap Method (MOM). *J. Phys. Chem. A* **2008**, *112*, 13164–13171.

(41) Hirata, S.; Head-Gordon, M. Time-dependent density functional theory within the Tamm–Dancoff approximation. *Chem. Phys. Lett.* **1999**, *314*, 291–299.

(42) (a) Silva-Junior, M. R.; Schreiber, M.; Sauer, S. P. A.; Thiel, W. Benchmarks for electronically excited states: Time-dependent density functional theory and density functional theory based multireference configuration interaction. *J. Chem. Phys.* **2008**, *129*, 104103. (b) Sears, J. S.; Koerzdoerfer, T.; Zhang, C. R.; Brédas, J.-L. Communication: Orbital instabilities and triplet states from time-dependent density functional theory and long-range corrected functionals. *J. Chem. Phys.* **2011**, *135*, 151103.

(43) (a) Sun, H. T.; Zhong, C.; Brédas, J.-L. Reliable Prediction with Tuned Range-Separated Functionals of the Singlet–Triplet Gap in Organic Emitters for Thermally Activated Delayed Fluorescence. *J. Chem. Theory Comput.* **2015**, *11*, 3851–3858. (b) Penfold, T. J. On predicting the excited-State properties of thermally activated delayed fluorescence emitters. *J. Phys. Chem. C* **2015**, *119*, 13535–13544.

(44) Lan, Z. G.; Lu, Y.; Weingart, O.; Thiel, W. Nonadiabatic Decay Dynamics of a Benzyldiene Malononitrile. *J. Phys. Chem. A* **2012**, *116*, 1510–1518.

(45) Shuai, Z. G.; Peng, Q. Excited states structure and processes: Understanding Organic Light-emitting Diodes at the Molecular Level. *Phys. Rep.* **2014**, *537*, 123–156.

(46) Wu, Q. Y.; Zhang, T.; Peng, Q.; Wang, D.; Shuai, Z. G. Aggregation Induced Blue-Shifted Emission-the Molecular Picture from a QM/MM Study. *Phys. Chem. Chem. Phys.* **2014**, *16*, 5545–5552.